

Spray-Assisted Deep-Frying Process for the In Situ Spherical Assembly of Graphene for Energy-Storage Devices

Sang-Hoon Park,[†] Hyun-Kyung Kim,[†] Seung-Beom Yoon,[†] Chang-Wook Lee,[†] Dongjoon Ahn,[‡] Sang-Ick Lee,[‡] Kwang Chul Roh,^{*,§} and Kwang-Bum Kim^{*,†}

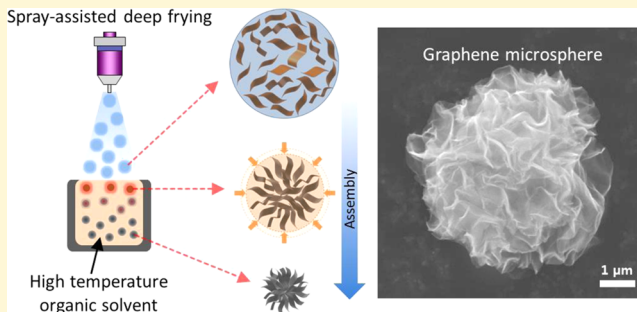
[†]Department of Materials Science and Engineering, Yonsei University 134 Shinchon-dong, Seodaemun-gu, Seoul 120-749, Republic of Korea

[‡]Advanced Battery Materials Team, GS Energy, 50, Seongnae-ro 6-gil, Gangdong-gu, Seoul, Republic of Korea

^{*}Energy Efficient Materials Team, Energy & Environmental Division, Korea Institute of Ceramic Engineering & Technology, 233-5 Gasan-Dong, Guemcheon-Gu, Seoul 153-801, Republic of Korea

Supporting Information

ABSTRACT: To take full advantage of graphene in macro-scale devices, it is important to integrate two-dimensional graphene nanosheets into a micro/macrosized structure that can fully utilize graphene's nanoscale characteristics. To this end, we developed a novel spray-assisted self-assembly process to create a spherically integrated graphene microstructure (graphene microsphere) using a high-temperature organic solvent in a manner reminiscent of deep-frying. This graphene microsphere improves the electrochemical performance of supercapacitors, in contrast to nonassembled graphene, which is attributed to its structural and pore characteristics. Furthermore, this synthesis method can also produce an effective graphene-based hybrid microsphere structure, in which Si nanoparticles are efficiently entrapped by graphene nanosheets during the assembly process. When used in a Li-ion battery, this material can provide a more suitable framework to buffer the considerable volume change that occurs in Si during electrochemical lithiation/delithiation, thereby improving cycling performance. This simple and versatile self-assembly method is therefore directly relevant to the future design and development of practical graphene-based electrode materials for various energy-storage devices.



INTRODUCTION

Electrochemical energy-storage devices have the potential to exhibit high energy density, high power density, and high cyclability, characteristics that will be required to meet the future demands for renewable energy, electric vehicles, and portable electronics.^{1,2} However, the rapid and widespread development of these applications means that further improvements are needed in the field of high-performance electrode materials.^{3,4} Among the various electrode materials available for energy storage devices, graphene, a one-atom-thick, two-dimensional (2D) sp² carbon structure, has attracted considerable interest as a next-generation electrode material. This can be attributed to a number of interesting properties of graphene, such as its good mechanical/chemical stability, high electrical/thermal conductivity, and a large surface area (over 2630 m² g⁻¹) because of its high surface-to-volume ratio.^{5–7} The combination of these unique physical and chemical properties means that graphene has significant potential to act as either an electrochemically active material in itself or as a conductive carbon template for hybrid/composite materials suitable for use in energy storage devices such as supercapacitors and Li-ion batteries.^{8–10}

Ever since the pioneering study by Ruoff et al. on the use of graphene electrodes in supercapacitors, and the work by Honma et al. on graphene-based nanohybrid anodes for Li-ion batteries, there have been extensive efforts directed toward developing graphene-based electrode materials for energy storage devices.^{9–12} When preparing graphene-based electrode materials, graphite oxide is generally considered the most suitable precursor for cost-effective mass production and for the structural/chemical modification of other active materials.^{13–15} However, previous studies have shown that the actual performance achieved is lower than that predicted on the basis of the ideal properties of graphene; this has been mainly attributed to the agglomeration and restacking of graphene nanosheets owing to their strong van der Waals interactions.^{14,15} Furthermore, because of the high aspect ratio of the 2D nanosheets, graphene tends to stack readily with a horizontal alignment during conventional electrode fabrication processes.¹⁶ This agglomeration/restacking tendency has a

Received: September 16, 2014

Revised: December 7, 2014

Published: December 21, 2014

negative effect on the specific capacitance (or specific capacity) and rate capability of electrodes, as the electrochemically active surface area of graphene is reduced by the presence of an interlayer spacing that is smaller than the electrolyte ions.⁸

Given these limitations, there is clearly a need to integrate graphene nanosheets into micro/macrosized structures that will allow the characteristic properties of graphene to be fully exploited.^{17,18} To this end, there has been a significant amount of research into the design of suitable architectures and the assembly of graphene nanosheet-based building blocks into desired structures with a controlled macroscale morphology. This has resulted in various strategies based on using sacrificial templates (such as ice crystals and colloidal particles), cross-linkers (sol–gel precursors, polymers, and ion linkages), or in situ self-assembly.^{19–25} Among these, the in situ self-assembly of graphene oxide (GO) has been recognized as one of the most powerful techniques because of its simplicity and versatility and because it allows for the fabrications of hybrid/composite structures using other nanomaterials.^{26–30} Moreover, by utilizing the transition in GO's intrinsic chemistry during solution-based reduction, this technique also allows for the self-assembly of GO nanosheets into a three-dimensional (3D) macroporous graphene hydrogel (or aerogel) that can provide mechanical robustness combined with an interconnected macroporous structure.³⁰ However, the direct use of the resulting macrostructure as an electrode in conventional cell configurations is still limited by its bulky size. In particular, the thickness of this macrostructure is typically on the millimeter or centimeter scale, making it difficult to accurately control its microscale thickness/tolerance. Moreover, the high pore volume resulting from the extremely large pore size (predominantly macropores) can greatly reduce the electrode density and the associated volumetric capacity (or capacitance).^{16,30} This also hinders its practical use as an electrode material in energy storage devices.

In a bid to develop a more suitable graphene structure for electrodes, we herein propose a strategy for the in situ self-assembly of 2D GO nanosheets into a micron-sized spherical graphene structure. To construct this “graphene microsphere,” we developed a novel spray-assisted self-assembly process that uses a high-temperature organic solvent; this process was inspired by the conventional process of deep-frying food. During this assembly process, henceforth referred to as “spray-assisted deep-frying,” the high-temperature organic solvent plays an important role in both the efficient assembly of the GO nanosheets into a graphene microstructure, as well as the creation of nanoporous channels inside this microstructure. This synthesis method can be used even in the presence of other active materials, thus allowing graphene-based hybrid microstructures to be fabricated. This study explores the possibility of creating silicon/graphene hybrid microspheres for use as Li-ion battery anodes, on the basis of the fact that silicon exhibits a theoretical specific capacity as high as 4200 mA h g⁻¹, a low operating potential, and low cost.^{31,32} This simple and versatile self-assembly method is therefore intended as a guide for engineers and scientists engaged in the rational design of graphene-based electrode materials for various electrochemical energy-storage devices.

■ EXPERIMENTAL SECTION

Synthesis of Graphene-Based Microspheres by a Spray-Assisted Deep-Frying Process. First, graphite oxide was prepared from bulk graphite flakes ($\sim 45\text{ }\mu\text{m}$, 99.99%, Aldrich) using a modified

Hummer's method.⁴⁰ The as-prepared graphite oxide was then exfoliated and dispersed in deionized water using a probe-type ultrasonicator at $\sim 5\text{ }^{\circ}\text{C}$ to obtain a stable 1.0 mg mL⁻¹ GO suspension. To ensure homogeneous ultrasonication, we magnetically stirred the dispersion continuously during exfoliation. The GO was then assembled into graphene microspheres using a spray-assisted deep-frying process (see the Supporting Information, Figure S1) that incorporated an ultrasonic-spray nozzle (Sono-Tek spray nozzle 8700, Sono-Tek Corp.) for the preparation of GO microdroplets, and a double-walled jacket containing an organic solvent (1-octanol or ethylene glycol, Aldrich) mixed with a reducing agent (L-ascorbic acid, Aldrich). In this jacket, the as-prepared aqueous GO suspension was injected at a flow rate of 50–200 mL h⁻¹ and atomized by the ultrasonic-spray nozzle to generate GO microdroplets. These GO microdroplets were sprayed downward into the organic solvent, which was maintained at a constant temperature of 110–160 °C and stirred continuously to reduce the temperature gradient and promote homogeneous assembly. The assembled graphene microspheres, which precipitated in the organic solvent, were collected and washed with acetone and water. After being dried overnight in a vacuum oven, the samples were then heat-treated at 600 °C in Ar gas to remove any residual functional groups present on the graphene microspheres.

Si-entrapped graphene microspheres were also synthesized from a Si/GO mixed suspension via the same spray-assisted deep-frying method. To prepare the Si/GO mixed suspension, we first dispersed Si nanoparticles ($\sim 100\text{ nm}$, GS Energy) in deionized water at a concentration of 2 mg mL⁻¹ by ultrasonication, and were then mixed homogeneously with a GO suspension in a GO/Si mass ratio of 1:1. This mixed suspension was sprayed downward into the organic solvent, which was maintained at a constant temperature of 160 °C. The resultant powder was washed and dried using the same procedure as that for the graphene microspheres.

Material Characterization. The morphologies and microstructures of the samples were observed by scanning electron microscopy (SEM) (S-4300E, Hitachi) and high-resolution transmission electron microscopy (HRTEM) (JEM-3010, JEOL). The structural properties of the samples during synthesis were examined by X-ray diffraction (XRD) analysis. X-ray photoelectron spectroscopy (XPS) was used to investigate the elemental compositions and the oxidation/reduction states of the carbon materials; an ESCA 2000 spectrometer (VG Microtech) was employed for the purpose. The surface area and pore characteristics of each sample were determined by analyzing their N₂ gas adsorption/desorption isotherms using the Brunauer–Emmett–Teller (BET) method (ASAP ZOZO, Micromeritics Co.). The pore size distributions were derived from the desorption branches of the isotherms using the Barrett–Joyner–Halenda (BJH) model.

The electrochemical properties of the graphene microspheres were investigated using a three-electrode cell with a platinum plate as the counter electrode and a saturated calomel electrode (SCE) as the reference electrode. The working electrode was prepared from a slurry mixture of 90 wt % active material and 10 wt % polyvinylidene fluoride (PVDF) dissolved in *N*-methyl-2-pyrrolidone (NMP) as a binder; this slurry was then coated onto a substrate and dried in a vacuum oven. Conductive additives such as carbon black were not added to the electrode, as the graphene-based material itself exhibited high electrical conductivity. Each working electrode had an area of 1 cm² (1 × 1 cm net area), and the amount of active material in the electrode was approximately 2 mg/cm². Cyclic voltammetry (CV) measurements were performed in an aqueous electrolyte solution of 1 M H₂SO₄ using a potentiostat–galvanostat (VMP3, Biologic) at potential scan rates of 10–500 mV s⁻¹ in a potential window of 0.0–0.9 V (vs SCE). The specific capacitance of the graphene electrode was subsequently calculated from the voltammetric charge, which was determined from the CV curves.

The electrochemical properties of the Si-entrapped graphene microspheres were investigated using 2032-type coin cells with a lithium foil counter electrode and 1 M LiPF₆ in ethylene carbonate/dimethyl carbonate/fluoroethylene carbonate (EC/DMC/FEC) (3:5:2 v/v) as the electrolyte. The working electrode was prepared from a mixture of 90 wt % Si-entrapped graphene microspheres and 10

wt % poly(acrylic acid) (PAA, Aldrich), used as a binder; the mixture was applied on a Cu foil. Each working electrode had an area of 1.13 cm² (punched into discs with $\phi = 12$ mm), and the amount of active material in the electrode was approximately 3 mg/cm². For comparison, electrodes were also prepared using mechanically blended Si/carbon black (Si/CB) and Si/graphene (Si/graphene) mixed with 50, 40, or 10 wt % binder. The specific capacities of all the electrodes were calculated from the total masses of Si and carbon, and their electrochemical characteristics were measured within a 2.5–0.001 V range using a potentiostat/galvanostat (VMP3, Biologic). Electrochemical impedance spectroscopy was performed using an impedance analyzer at a DC bias voltage of 0.2 V and AC frequencies ranging from 200 kHz to 10 mHz.

RESULTS AND DISCUSSION

The proposed spray-assisted deep-frying process for the synthesis of graphene microspheres is illustrated in Figure 1a. Note that this is quite similar to the conventional deep-frying of croquettes, in that a minced filling (building block) is first shaped into a suitable form (desired shape during assembly), coated with breadcrumbs (structure directing-agent), and then deep fried in oil at a temperature of over 160 °C (the assembly process). The desired spherical microdroplet-like shape during assembly was achieved in this instance by the ultrasonic spraying of an aqueous GO suspension, which momentarily creates a spherical microreactor analogous to a water/oil (W/O) microemulsion system (see Experimental Details and Supporting Information, Figure S1, for the equipment configuration).

Images b and c in Figure 1 show SEM images of the synthesized graphene microspheres. It can be seen from the images that the crumpled 2D nanosheets acted as basic building blocks and assembled successfully into a spherical microstructure with a uniform size of $\sim 5 \mu\text{m}$ on the macroscopic scale. (The lateral size of the individual nanosheets was 1–2 μm ; see the Supporting Information, Figure S2.) Plan-view of the TEM image (Figure 1d) and the surface SEM image (Figure 1f) of a graphene microsphere show that the nanosheets at the surface of the microsphere are typically oriented in the outward direction with respect to the microsphere's outer surface; this corresponds well with the scheme shown in Figure 1d. The structure of this microsphere is quite analogous to an urchin or a flower. More importantly, cross-sectional (Figure 1g, h) TEM images of a microsphere show that these microspheres possessed aligned nanoporous channels, which were formed by the unique arrangement of the individual 2D nanosheets; these channels were arranged radially in an outward direction relative to the microsphere's outer surface, as indicated by the arrows in Figure 1f.

Figure 2 shows the dependence of the graphene microstructure on the synthesis conditions, which include the type of organic solvent used (polar or nonpolar), its temperature, and whether or not it contains a reducing agent (assembly agent). It is evident from this that a reducing agent such as L-ascorbic acid is required to assemble a spherical microstructure from GO building blocks, with subsequent creation of reduced graphene oxide (rGO) and increase in the van der Waals interactions between adjacent graphene sheets.^{26,27,30} In the absence of a reducing agent (Figure 2a), the sprayed GO microdroplets did not assemble into a microsphere, but rather redispersed into the organic solvent (inset photographic image) and stacked to form the paperlike structure observed after collection by filtration (inset SEM image). The XRD pattern of the resultant sample (inset within the SEM image of Figure 2a) shows

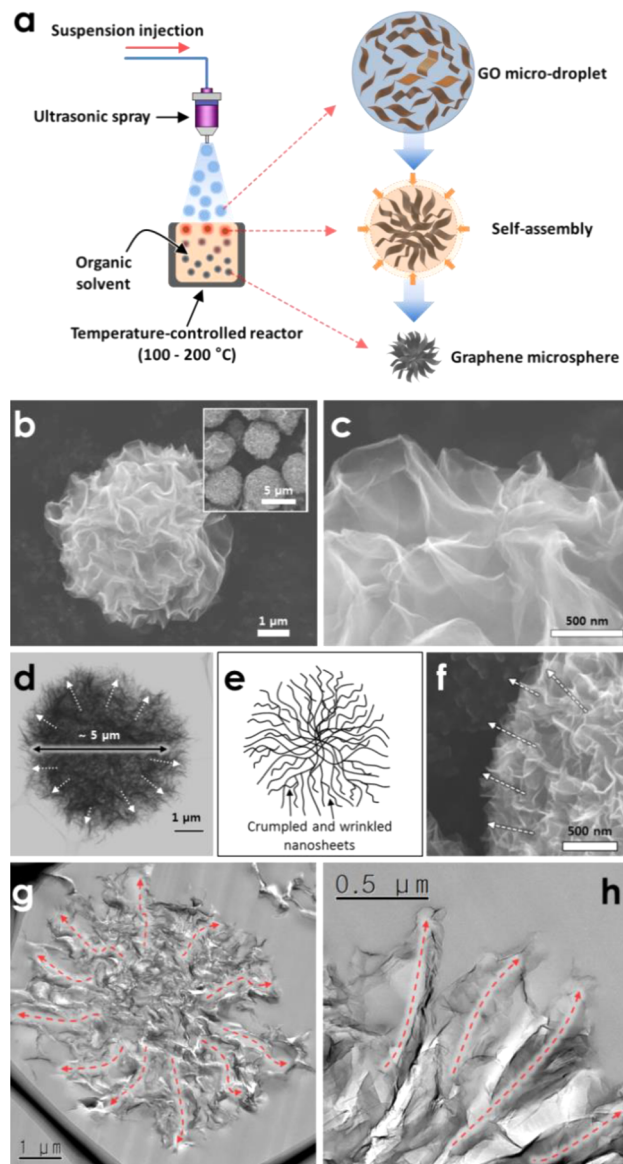


Figure 1. (a) Synthesis of graphene microspheres by the spray-assisted deep-frying process. (b) Low-magnification and (c) high-magnification SEM images of the graphene microspheres. (d) Plan-view TEM image. (e) Schematic model of a microsphere assembled from crumpled graphene nanosheets. (f) SEM image of the surface of graphene microsphere. (g) Low-magnification and (h) high-magnification cross-sectional TEM images.

characteristic GO peaks at $2\theta = 10^\circ$.¹³ The broad peak at $2\theta = 26^\circ$ may be due to the partial reduction of GO by the organic solvent at 160 °C.

The immiscibility of the organic solvent and the sprayed GO suspension is an important factor in generating the microspheres. Figure 2b shows the result of spraying this GO suspension into ethylene glycol, a polar organic solvent that is miscible with the aqueous GO microdroplets; here, the ethylene glycol was maintained at 160 °C and contained L-ascorbic acid as a reducing agent. The XRD pattern of this sample (inset of the SEM image in Figure 2b) contains a primary diffraction peak at $2\theta = 26^\circ$, indicating the efficient reduction of GO; however, the SEM image revealed a nonassembled, randomly agglomerated structure consisting of graphene nanosheets and similar to that of chemically reduced

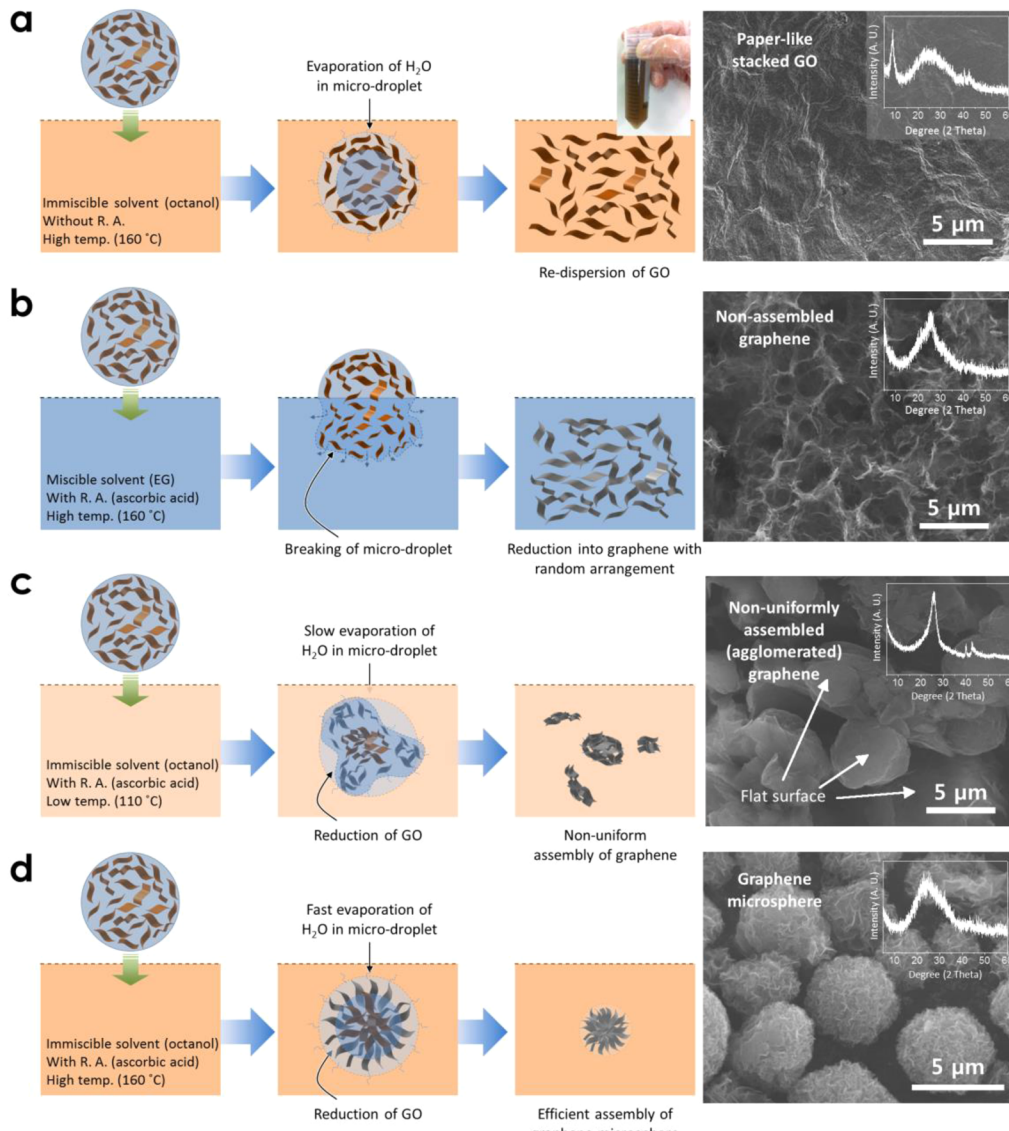


Figure 2. Assembly of graphene microspheres through the spray-assisted deep-frying process under different conditions. Schematic illustration and SEM images of samples prepared using (a) a nonpolar solvent (1-octanol) maintained at 160 °C and not containing a reducing agent, (b) polar solvent (ethylene glycol) maintained at 160 °C and containing a reducing agent (L-ascorbic acid), and (c) 1-octanol maintained at a relatively low temperature of 110 °C and containing a reducing agent. (d) Schematic illustration and SEM image of graphene microspheres prepared under optimal conditions (1-octanol maintained at 160 °C and containing L-ascorbic acid as a reducing agent).

GO (rGO). This is attributed to the fact that the polarity of the aqueous GO microdroplets allows them to blend with the ethylene glycol, thereby losing their spherical shape and randomly dispersed within the solvent.

Even if a nonpolar organic solvent containing a reducing agent (1-octanol with L-ascorbic acid) is used, the individual nanosheets in the microdroplet are not uniformly assembled when only a relatively low temperature (110 °C) is used (Figure 2c). This can be explained by a decrease in the evaporation rate of the aqueous microdroplets, as well as the rate of GO reduction within the droplet; these factors, in turn, degrade the uniformity of the final assembled structure. The conventional deep-frying analogy can illustrate this effect clearly: lower temperatures increase the probability of cracks forming on the surface of the fried food. Likewise, a similar effect can occur with the aqueous GO microdroplets. More importantly, a low temperature results in the majority of the

particles having a flat surface, instead of the arrangement of nanosheets in a radially outward manner. This is attributable to GO's amphiphilic nature.^{33,34} Specifically, a low temperature (or more precisely a low microdroplet evaporation rate) can provide sufficient time for the randomly dispersed GO sheets to be aligned along the water droplet/organic solvent interface, owing to their surfactant-like function in W/O systems. This ultimately creates a flat surface by exposing the graphene basal plane along the circular direction of the interface. In this case, the surface morphology is similar to that of graphene (or GO) spheres previously prepared using a W/O emulsion or sacrificial templates.^{34–36} On the other hand, when the temperature of the nonpolar organic solvent is 160 °C (Figure 2d), the GO in the microdroplet effectively assembles into uniform ball-like structures with a radial arrangement. The high temperature of the organic solvent increases the evaporation rate of the water inside the sprayed microdroplets, and the water vapor produced

tends to escape outward, as its density is lower than that in the liquid state. This rapid evaporation of water in the high-temperature organic solvent is believed to be the cause of the nanochannels radiating outward between the assembled nanosheets inside the final structure (also see the Supporting Information, Figure S3, for a schematic showing the arrangement of outwardly radiating nanosheets in a microsphere).

Since the arrangement of graphene nanosheets can greatly influence the surface area and pore characteristics of a microstructure, the BET surface area and the BJH pore size distributions were obtained for each sample. From the results shown in Figure 3, it is apparent that the graphene

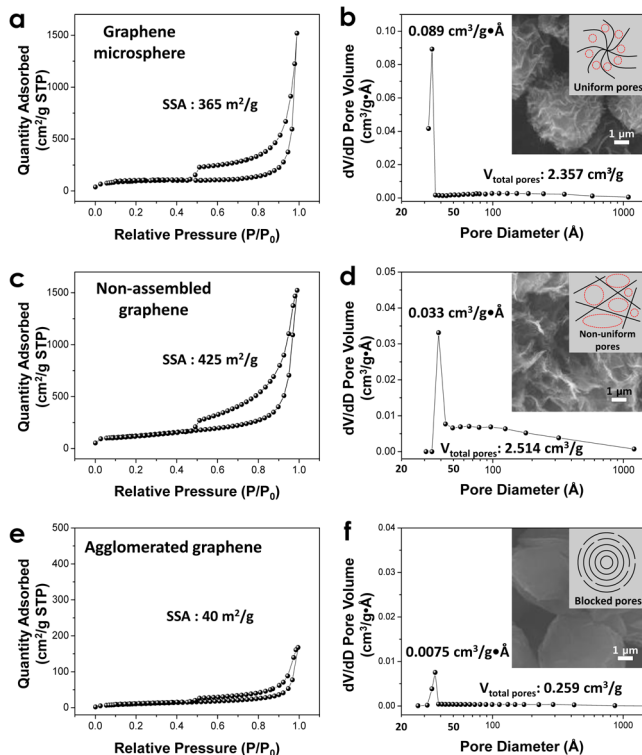


Figure 3. Nitrogen adsorption/desorption isotherms and BJH pore size distributions of (a, b) graphene microspheres, (c, d) non-assembled graphene, and (e, f) agglomerated graphene. (insets, right column: schematic models for the arrangement of the graphene nanosheets relative to the sample SEM images).

microspheres exhibit a typical type-IV isotherm with H2 hysteresis loops (Figure 3a); this isotherm is similar to the characteristic isotherm of nonassembled graphene (Figure 3c; simple rGO).¹³ The specific surface area of the graphene microsphere ($365 \text{ m}^2 \text{ g}^{-1}$) was slightly less than that of the nonassembled graphene ($425 \text{ m}^2 \text{ g}^{-1}$); however, as shown in Figure 3b, d, the graphene microsphere possesses a far more uniform pore size. Although the pore size of the nonassembled graphene is widely distributed within 3–100 nm (mainly 3.84 nm, Figure 3d), the graphene microsphere exhibits a narrow pore size distribution, with most of the pores being 3.42 nm (Figure 3b). This was proof of the formation of a more uniform pore structure in graphene microsphere.³⁷ More interestingly, despite the lower total pore volume (pore volume of the total number of pores, $V_{\text{total pores}}$) of the graphene microsphere ($V_{\text{total pores}}$ of graphene microsphere: $2.357 \text{ cm}^3 \text{ g}^{-1}$ and $V_{\text{total pores}}$ of nonassembled graphene: $2.514 \text{ cm}^3 \text{ g}^{-1}$), the graphene microsphere exhibits a significantly higher pore

volume at the main pore diameter ($0.089 \text{ cm}^3 \text{ g}^{-1} \text{ Å}^{-1}$ at a pore diameter of 34.2 Å) than that of nonassembled graphene ($0.033 \text{ cm} \text{ g}^{-1} \text{ Å}^{-1}$ at a pore diameter of 38.4 Å). These results strongly support the conclusion that the graphene microsphere possesses a more uniform pore structure, owing to the arrangement of the 2D nanosheets, as shown in the insets of Figure 3b, d.³⁸ In contrast, the agglomerated graphene prepared at 110 °C (nonuniformly assembled graphene, Figure 2c) exhibits both the lowest surface area ($40 \text{ m}^2 \text{ g}^{-1}$) and the lowest pore volume (Figure 3e, f). This is likely the result of its pores being blocked by the circularly stacked graphene nanosheets (inset in Figure 3f) and demonstrates that an outwardly radiating nanosheet arrangement creates more open channels and allows the inner surfaces of the microstructure to be effectively utilized.

To determine the elemental compositions and graphene reduction levels of the samples, XPS analyses were performed. The atomic concentrations of C and O in the as-prepared graphite oxide were determined through wide-scan XPS (Figure 4a) to be 62 and 35.2%, respectively; these correspond to a C/

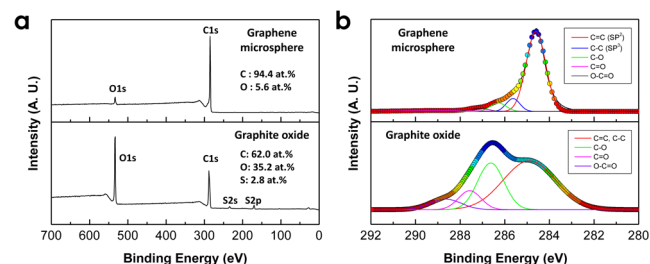


Figure 4. (a) Wide-scan XPS and (b) deconvoluted XPS C 1s spectra of graphite oxide and a graphene microsphere.

O ratio of 1.76. Following the assembly of the graphene microsphere, the O 1s peak was significantly reduced and the C/O ratio increased to 16.9; this could be attributed to the removal of oxygen functionalities by the reduction of GO to rGO.²⁷ Figure 4b shows the deconvoluted XPS C 1s spectra of graphite oxide and a graphene microsphere, with both showing typical components of C=C/C-C (sp² and sp³, ~284.6 eV), C-O (hydroxyl and epoxy, ~286.5 eV), and C=O (carbonyl, ~287.8 eV).³⁹ The relative atomic percentages of the sp²/sp³ carbons and oxygen-containing functional groups are listed in Table S1 in the Supporting Information. It can be seen that the as-prepared graphite oxide contained 56.3% sp²/sp³ carbon components and 43.7% heterocarbon components (arising from oxygen-containing functional groups such as C—O, C=O, and O—C=O). In comparison, the graphene microsphere contained 86.2% sp²/sp³ carbon components and 13.8% heterocarbon components; this confirms that GO is reduced to graphene during the spray-assisted deep-frying process.

Figure 5 compares the electrochemical properties of graphene microspheres, nonassembled graphene, and agglomerated graphene electrodes. The rectangular shape of the CV curve of a graphene microsphere-based electrode (Figure 5a) at a scan rate of 10 mV s⁻¹ is indicative of electrical double-layer capacitance (EDLC) behavior. When the scan rate was increased to 500 mV s⁻¹, the CV curve maintained its rectangular shape, suggesting a high-rate capability induced by fast charge transport within the uniform pore structure of the microsphere. In Figure 5b, it is shown that the specific capacitance of the graphene microsphere-based electrode at a

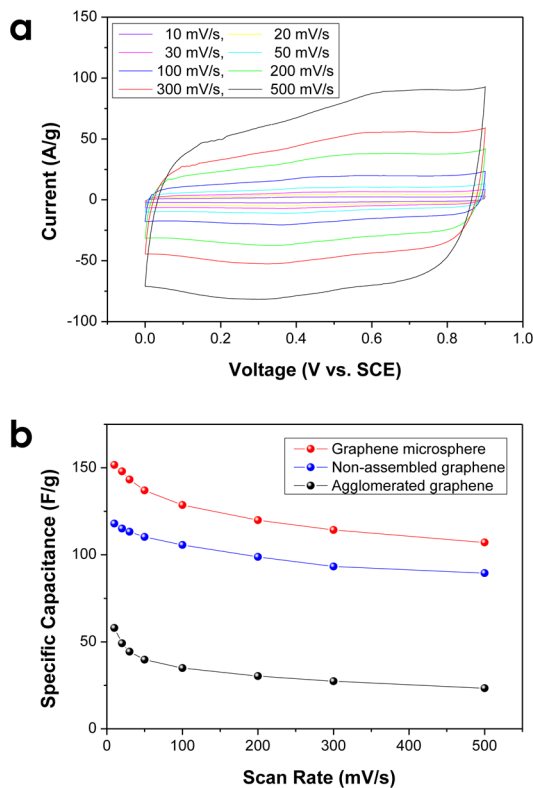


Figure 5. (a) CV curves at various scan rates of a graphene microsphere and (b) specific capacitances and rate capabilities of graphene microsphere-, nonassembled graphene-, and agglomerated graphene-based electrodes in 1 M H_2SO_4 aqueous electrolyte.

scan rate of 10 mV s^{-1} (151 F g^{-1}) is significantly higher than that of a nonassembled graphene-based electrode (118 F g^{-1}) and an agglomerated graphene-based electrode (58 F g^{-1}) (see the Supporting Information, Figure S4, for the CVs of nonassembled graphene and agglomerated graphene electrodes). Because the EDLC performance of carbon materials is reported to be highly dependent on their structural properties, particularly their surface area and porosity.^{8–10} The poor electrochemical performance of the agglomerated graphene-based electrode is considered to be directly caused by its low specific surface area ($40 \text{ m}^2 \text{ g}^{-1}$) and blocked-pore structure. On the other hand, even though the graphene microsphere has a lower surface area ($365 \text{ m}^2 \text{ g}^{-1}$) than that of the nonassembled simple graphene ($425 \text{ m}^2 \text{ g}^{-1}$), the electrode based on the former nevertheless exhibited a superior electrochemical performance.

This can be explained by the aforementioned paper-like stacking of the individual nanosheets in the nonassembled graphene, because of the high aspect ratio of the nanosheets (see the Supporting Information, Figure S5a); this has a negative effect on their electrochemical properties.¹⁶ In contrast, the graphene microsphere maintains its initial morphology after electrode fabrication (see the Supplementary Figure S5b), thereby providing a higher electrochemically active surface area. When the scan rate was increased to 500 mV s^{-1} , the specific capacitance of the graphene microsphere-based electrode decreased slightly to 107 F g^{-1} , thus highlighting the competitive rate capability among graphene-based electrodes (see the Supporting Information, Figure S6, for the specific capacitance of a graphene microsphere as measured by the

galvanostatic charge–discharge method using a two-electrode cell).

To determine the applicability of the spray-assisted deep-frying process for the synthesis of hybrid electrode materials for Li-ion batteries, we employed it to assemble Si-entrapped graphene microspheres (Si/graphene microspheres) by using a uniformly dispersed mixed suspension of Si nanoparticles and GO (Figure 6a). The SEM and TEM images of the resulting

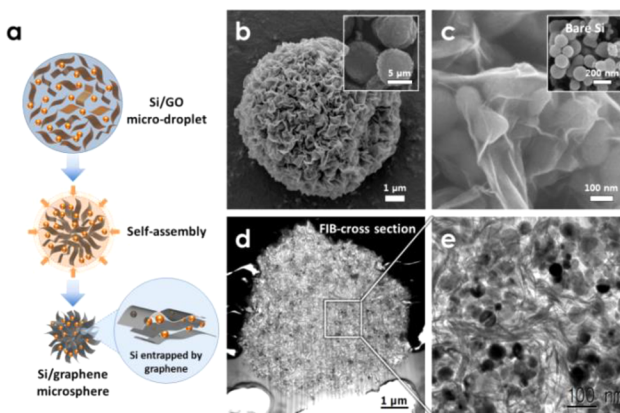


Figure 6. (a) Schematic depicting the synthesis of a Si-entrapped graphene microsphere (Si/graphene microsphere). (b) SEM image of a single Si/graphene microsphere (inset shows a low-magnification SEM image). (c) High-magnification SEM of the Si/graphene microsphere surface (inset shows a bare Si nanoparticle with a size of $\sim 100 \text{ nm}$). (d) Cross-sectional TEM image of a Si/graphene microsphere and (e) a magnified view of the core structure of the microsphere in d.

structure shown in Figures 6b–e confirm that even in the presence of other nanoparticles, GO can still successfully assemble into a microsphere. Furthermore, closer inspection (Figure 6c) reveals that the Si nanoparticles, which are $100\text{--}200 \text{ nm}$ in size (see inset SEM image), become wrapped in the graphene nanosheets. Cross-sectional TEM analysis of focused ion beam (FIB)-etched samples (Figures 6d and 6e) also reveal that the Si nanoparticles were evenly dispersed not only near the microsphere surface, but also within the microsphere itself (Figure 6e). This demonstrates that the nanoparticles are efficiently entrapped by the graphene nanosheets during the assembly process.

The structure and chemical composition of the Si/graphene microspheres were investigated by XRD and XPS analyses and thermogravimetric analysis (TGA). The XRD peak positions of the Si/graphene microsphere (Figure 7a) are identical to the characteristic peaks of both graphene and Si, further confirming that the Si nanoparticles were embedded within the reduced graphene structure. From the results of wide-scan XPS, the atomic concentrations of C, O, and Si were determined to be 83.9, 11.5, and 4.6, respectively (Figure 7b). The Si concentration is markedly lower than the value expected on the basis of the Si/GO mass ratio of 1:1 in the original mixed suspension; that is, if the weight loss accompanying the reduction of GO to rGO is taken into account ($\sim 40\%$ weight loss after the removal of the oxygen-containing functional groups), then the Si content of the resultant Si/graphene microsphere should be on the order of $\sim 62.5 \text{ wt } \%$. However, given the limited depth resolution of XPS (usually $\sim 10 \text{ nm}$), it is possible that this discrepancy is simply due to the entrapment of the Si nanoparticles within the assembled graphene

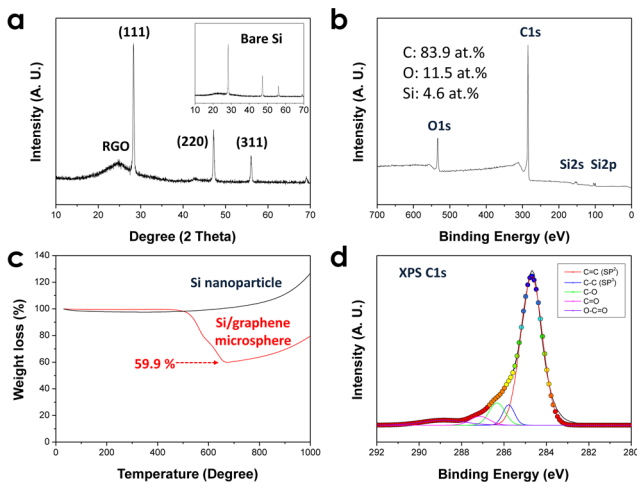


Figure 7. (a) XRD pattern of a Si/graphene microsphere (inset shows the XRD pattern of bare Si nanoparticles). (b) Wide-scan XPS spectrum of a Si/graphene microsphere. (c) TGA curves of Si/graphene microspheres and bare Si nanoparticles in air. (d) Deconvoluted XPS C 1s spectrum of a Si/graphene microsphere.

nanosheets. To confirm this, the Si content of the Si/graphene microsphere was evaluated with greater accuracy by using TGA (Figure 7c). It was found that the carbon-based weight loss of the Si/graphene microsphere is 40.1% at 630 °C, indicating a 59.9 wt % Si content in the hybrid material, a value that is close to the estimated value. The XPS C 1s spectra of the Si/graphene microsphere indicated the presence of 82.5% sp²/sp³ carbon components and 17.5% heterocarbon components, indicating that the GO reduction level was high and should provide a highly conductive network for the Si nanoparticles.

The electrochemical properties of the Si/graphene microsphere structure were measured using a 2032-type coin cell with a Li-metal counter electrode and compared with those of Si/CB and nonassembled Si/graphene (Si/graphene mixture) electrodes. The galvanostatic charge–discharge curves obtained during initial lithiation/delithiation at a constant current density of 500 mA g⁻¹ is clear from these results that the graphene-based electrodes (i.e., the Si/graphene microspheres and Si/graphene mixture electrodes) possess higher discharge/charge capacities than does the Si/CB electrode (first discharge and charge capacities of 1400 and 1108 mA h g⁻¹, respectively), thereby confirming that the 2D nanosheets of graphene provide an efficient conducting/buffering framework for the Si nanoparticles.³⁹ It should also be noted that even though the initial discharge capacity of the Si/graphene microsphere-based electrode (1632 mA h g⁻¹) was slightly lower than that of the Si/graphene mixture-based electrode (1729 mA h g⁻¹), its retained charge capacity during subsequent delithiation was higher (1364 mA h g⁻¹ for the microspheres vs 1243 mA h g⁻¹ for the mixture). As a result, the Coulombic efficiency of the Si/graphene microsphere-based electrode during the initial lithiation/delithiation (83.5%) was clearly greater than those of the other two electrodes. Generally, a low initial Coulombic efficiency in anode materials can be attributed to an irreversible capacity loss caused by the formation of a solid electrolyte interface (SEI) between the electrode material and the electrolyte during lithiation at voltages lower than 1.0 V vs Li/Li⁺.³¹ Thus, in a conventional Si anode, the pulverization of the Si owing to its high volume expansion creates a newly exposed electrolyte interface, thereby promoting the formation

of an irreversible SEI. In contrast, the entrapment of the Si nanoparticles in the Si/graphene microspheres reduces their direct exposure to the electrolyte during lithiation/delithiation (even after pulverization), leading to a stable interface and increased Coulombic efficiency.

The dQ/dV profiles of the electrodes during their initial lithiation/delithiation (Figure 8b) provide further evidence of

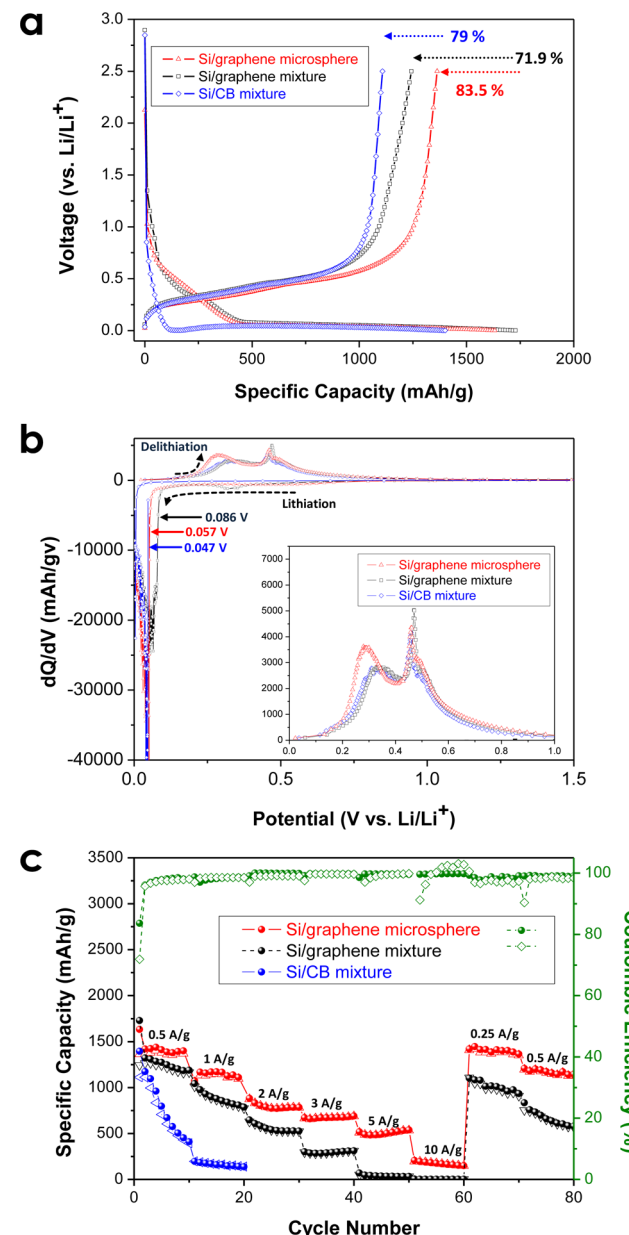


Figure 8. (a) Initial discharge/charge profiles, (b) dQ/dV differential profiles, and (c) cycling performances at various current densities between 0.5 and 10 A g⁻¹ of the Si/graphene microsphere-, Si/graphene mixture-, and Si/CB mixture-based electrodes (electrolyte: 1 M LiPF₆ in EC/DMC/FEC).

the structural advantage of the Si/graphene microsphere. All of the Si-based electrodes show a characteristic peak voltages lower than 0.1 V during the first lithiation cycle, and two peaks, at 0.4 and 0.5 V, respectively, during subsequent delithiation; these can be attributed to the formation and dealloying of a Li–Si alloy phase, respectively. However, there is a notable

difference between the electrodes in terms of the potential at which these peaks appear. During the first lithiation of the Si/graphene mixture-based electrode, the formation of a Li–Si alloy phase, as evidenced by the cathodic peak, occurs at a higher potential (0.086 V) than that in the case of the other electrodes (0.057 V for the Si/graphene microsphere-based electrode and 0.047 V for the Si/CB electrode). This result indicates that the lowest cathodic overpotential was induced for the Si/graphene mixture-based electrode during the first lithiation process. More interesting, despite the graphene contents of the graphene-containing electrodes (Si/graphene mixture and Si/graphene microsphere electrodes) being similar, the Si/graphene mixture electrode exhibited a lower cathodic overpotential than did the Si/graphene microsphere-based electrode. At the time, the mechanically blended Si/graphene mixture might possess a more open structure for the movement of the Si nanoparticles to the electrolyte ion than that in the case of the Si-entrapped graphene microsphere (wrapped structure). Therefore, during the first lithiation, the Si/graphene mixture-based electrode exhibited a lower cathodic overpotential than that of the Si/graphene microsphere electrode; this might be due to the efficient mass transfer of Li ions to the Si nanoparticles by the relatively open framework in the mechanically blended electrodes. On the other hand, this tendency was reversed in case of the following delithiation process. Conversely, the dealloying of this Li–Si phase, represented by the anodic peak, initially occurs at a lower potential for the Si/graphene microsphere electrode (inset in Figure 8b), thus indicating that a relatively low anodic overpotential was induced during delithiation. These results demonstrate clearly that the efficiently wrapped structure of the Si/graphene microsphere produces a substantially more stable conducting network. In general, during the first lithiation process, Si undergoes a volume expansion of approximately 400% because of the formation of a Li–Si alloy phase, which causes the electrode to lose contact and increases its electronic resistance.^{31,32} The Si-entrapped structures in the Si/graphene microsphere-based electrode could produce a more stable conducting network than those of the other mechanically blended mixture-based electrodes. Thus, this network with high electronic conductivity was better maintained even after the first lithiation process, which was accompanied by a 400% increase in the Si volume. Therefore, during the subsequent delithiation process, the Si/graphene microsphere-based electrode could exhibit the lowest anodic overpotential because of its stable conducting network, which resulted in higher electronic conductivity.

Figure 8c shows the charge/discharge capacities and associated Coulombic efficiencies of the Si/graphene microsphere, Si/graphene mixture, and Si/CB electrodes cycled at various current densities. It can be seen from the figure that the cycling performance of the Si/CB electrode is much lower than those of the Si/graphene microsphere- and Si/graphene mixture-based electrodes. Moreover, although the charge/discharge capacities of both graphene-containing electrodes are similar at the beginning of each cycle (1–3 cycles), the capacity of the Si/graphene mixture-based electrode decreases markedly with further cycling. The Si/graphene microsphere electrode, on the other hand, not only exhibits enhanced cyclability, but also has a better rate capability when the current density is increased from 0.5 to 10 A g⁻¹. Furthermore, the discharge capacities of the graphene microsphere-based electrode were 1398, 784, and 537 mA h g⁻¹ at 0.5 (after 10

cycles), 2 (after 30 cycles), and 5 A g⁻¹ (after 50 cycles), respectively; these values are significantly higher than those of the Si/graphene mixture-based electrode (1187, 527, and 32 mA h g⁻¹ at 0.5, 2, and 5 A g⁻¹, respectively). The Si/graphene microsphere-based electrode also exhibited a stable Coulombic efficiency of up to 99% after 2 cycles. Further, when its current density was decreased to 0.25 and 0.5 A g⁻¹, its discharge capacity increased to 1364 and 1145 mA h g⁻¹, respectively. The fact that these values are much higher than those for the Si/graphene mixture-based electrode (934 and 579 mA h g⁻¹) confirms that the Si entrapped in the graphene sheet microspheres is far more effective in providing a buffering/conducting network than is the simple mixing of the two materials. In addition, the Si-entrapped graphene microsphere-based electrode showed an electrode density of 1.16 g/cm³. Thus, the volumetric capacity of the Si/graphene microsphere electrode at a low current density (0.5 A/g) was calculated and found to be 1500–1650 mA h/cm³, which is more than three times higher than that of conventionally used graphite anodes (volumetric capacity of graphite: ~483 mA h/cm³ = 372 mA h/g (theoretical gravimetric capacity) × ~1.3 g/cm³ (typical electrode density)). The electrochemical impedance spectroscopy results also support the conclusion that a microsphere electrode can provide a more stable network during lithiation/delithiation (see the Supporting Information, Figure S6, for the Nyquist plots of the Si/graphene microsphere- and mixture-based electrodes).

■ CONCLUSIONS

A simple, spray-assisted method for the self-assembly of graphene was successfully demonstrated by using a high-temperature organic solvent in a manner reminiscent of the deep-frying of food. In this method, an aqueous suspension of GO is sprayed into a nonpolar organic solvent (1-octanol) that contains a reducing agent (L-ascorbic acid) and is held at a temperature of 160 °C. The high temperature of the nonpolar organic solvent plays an important role in the assembly of the sprayed GO nanosheets into graphene microspheres and the creation of nanoporous channels inside the resulting microstructure. These graphene microspheres exhibit improved electrochemical performance in terms of specific capacitance and rate capability; this is attributed to their structural and pore characteristics. This synthesis method can also be used for fabricating graphene-based hybrid microstructures (Si/graphene microspheres) suitable for use in Li-ion batteries. The resulting hybrid material, which consists of a spherical structure in which Si nanoparticles are entrapped between graphene layers, provides a more efficient framework for buffering the significant volume change (up to 400%) that occurs in Si during electrochemical lithiation/delithiation. Consequently, a Si/graphene microsphere-based electrode exhibits significantly improved cycling performance and a higher rate capability than that of a simple Si/graphene mixture-based electrode. This versatile self-assembly method therefore has direct relevance to the future design and practical development of graphene-based electrode materials for various electrochemical energy-storage and conversion devices.

■ ASSOCIATED CONTENT

S Supporting Information

Figure S1, photographic images of the experimental equipment; Figure S2, structural properties of graphene oxide nanosheets; Figure S3, scheme for the assembly of nanosheets in a grapheme

microsphere; Figure S4, CV curve for nonassembled graphene and agglomerated graphene electrodes; Figure S5, SEM images of electrodes; Figure S6, galvanostatic charge–discharge curves of the symmetric two-electrode cell using graphene microsphere; Figure S7, Nyquist plots of the electrodes; Tables S1 and S2, XPS C 1s peak position and relative atomic percentages of the various samples. This material is available free of charge via the Internet at <http://pubs.acs.org>.

AUTHOR INFORMATION

Corresponding Authors

*E-mail: rkc@kicet.re.kr.

*E-mail: kbjkim@yonsei.ac.kr.

Author Contributions

The manuscript was written with contributions from all authors. All authors have given approval to the final version of the manuscript.

Notes

The authors declare no competing financial interest.

ACKNOWLEDGMENTS

This work was supported by the Energy Efficiency and Resources Program of the Korea Institute of Energy Technology Evaluation and Planning (KETEP), under grants funded by the Ministry of Knowledge Economy, Korea (20122010100140 and 2010T100200232).

REFERENCES

- (1) Poizot, P.; Laruelle, S.; Grugeon, S.; Dupont, L.; Tarascon, J. M. *Nature* **2000**, *407*, 496.
- (2) Tarascon, J. M.; Armand, M. *Nature* **2001**, *414*, 359.
- (3) Arico, A. S.; Bruce, P.; Scrosati, B.; Tarascon, J. M.; Van Schalkwijk, W. *Nat. Mater.* **2005**, *4*, 366.
- (4) Manthiram, A.; Murugan, A. V.; Sarkar, A.; Muraliganth, T. *Energy Environ. Sci.* **2008**, *1*, 621.
- (5) Novoselov, K. S.; Geim, A. K.; Morozov, S. V.; Jiang, D.; Zhang, Y.; Dubonos, S. V.; Grigorieva, I. V.; Firsov, A. A. *Science* **2004**, *306*, 666.
- (6) Novoselov, K. S.; Geim, A. K.; Morozov, S. V.; Jiang, D.; Katsnelson, M. I.; Grigorieva, I. V.; Dubonos, S. V.; Firsov, A. A. *Nature* **2005**, *438*, 197.
- (7) Geim, A. K.; Novoselov, K. S. *Nat. Mater.* **2007**, *6*, 183.
- (8) Huang, Y.; Liang, J. J.; Chen, Y. S. *Small* **2012**, *8*, 1805.
- (9) Wu, Z. S.; Zhou, G. M.; Yin, L. C.; Ren, W.; Li, F.; Cheng, H. M. *Nano Energy* **2012**, *1*, 107.
- (10) Xu, C. H.; Xu, B. H.; Gu, Y.; Xiong, Z. G.; Sun, J.; Zhao, X. S. *Energy Environ. Sci.* **2013**, *6*, 1388.
- (11) Stoller, M. D.; Park, S. J.; Zhu, Y. W.; An, J. H.; Ruoff, R. S. *Nano Lett.* **2008**, *8*, 3498.
- (12) Paek, S. M.; Yoo, E.; Honma, I. *Nano Lett.* **2009**, *9*, 72.
- (13) Stankovich, S.; Dikin, D. A.; Piner, R. D.; Kohlhaas, K. A.; Kleinhammes, A.; Jia, Y.; Wu, Y.; Nguyen, S. T.; Ruoff, R. S. *Carbon* **2007**, *45*, 1558.
- (14) Pei, S. F.; Cheng, H. M. *Carbon* **2012**, *50*, 3210.
- (15) Park, S.; Ruoff, R. S. *Nat. Nanotechnol.* **2009**, *4*, 217.
- (16) Luo, J. Y.; Jang, H. D.; Huang, J. X. *ACS Nano* **2013**, *7*, 1464.
- (17) Chen, Z. P.; Ren, W. C.; Gao, L. B.; Liu, B. L.; Pei, S. F.; Cheng, H. M. *Nat. Mater.* **2011**, *10*, 424.
- (18) Liu, F.; Seo, T. S. *Adv. Funct. Mater.* **2010**, *20*, 1930.
- (19) Vickery, J. L.; Patil, A. J.; Mann, S. *Adv. Mater.* **2009**, *21*, 2180.
- (20) Choi, B. G.; Yang, M.; Hong, W. H.; Choi, J. W.; Huh, Y. S. *ACS Nano* **2012**, *6*, 4020.
- (21) Wang, X. L.; Bai, H.; Yao, Z. Y.; Liu, A. R.; Shi, G. Q. *J. Mater. Chem.* **2010**, *20*, 9032.
- (22) Bai, H.; Sheng, K. X.; Zhang, P. F.; Li, C.; Shi, G. Q. *J. Mater. Chem.* **2011**, *21*, 18653.
- (23) Bai, H.; Li, C.; Wang, X. L.; Shi, G. Q. *Chem. Commun.* **2010**, *46*, 2376.
- (24) Worsley, M. A.; Pauzauskie, P. J.; Olson, T. Y.; Biener, J.; Satcher, J. H.; Baumann, T. F. *J. Am. Chem. Soc.* **2010**, *132*, 14067.
- (25) Cong, H. P.; Ren, X. C.; Wang, P.; Yu, S. H. *ACS Nano* **2012**, *6*, 2693.
- (26) Sheng, K. X.; Xu, Y. X.; Li, C.; Shi, G. Q. *New Carbon Mater.* **2011**, *26*, 9.
- (27) Chen, W. F.; Yan, L. F. *Nanoscale* **2011**, *3*, 3132.
- (28) Chabot, V.; Higgins, D.; Yu, A. P.; Xiao, X. C.; Chen, Z. W.; Zhang, J. *J. Energy Environ. Sci.* **2014**, *7*, 1564.
- (29) Zhang, L. B.; Chen, G. Y.; Hedhili, M. N.; Zhang, H. N.; Wang, P. *Nanoscale* **2012**, *4*, 7038.
- (30) Li, C.; Shi, G. Q. *Nanoscale* **2012**, *4*, 5549.
- (31) Wu, H.; Cui, Y. *Nano Today* **2012**, *7*, 414.
- (32) Park, M. H.; Kim, M. G.; Joo, J.; Kim, K.; Kim, J.; Ahn, S.; Cui, Y.; Cho, J. *Nano Lett.* **2009**, *9*, 3844.
- (33) Tang, Z. H.; Zhuang, J.; Wang, X. *Langmuir* **2010**, *26*, 9045.
- (34) Guo, P.; Song, H. H.; Chen, X. H. *J. Mater. Chem.* **2010**, *20*, 4867.
- (35) Hong, J.; Char, K.; Kim, B. S. *J. Phys. Chem. Lett.* **2010**, *1*, 3442.
- (36) Yoon, S. M.; Choi, W. M.; Baik, H.; Shin, H. J.; Song, I.; Kwon, M. S.; Bae, J. J.; Kim, H.; Lee, Y. H.; Choi, J. Y. *ACS Nano* **2012**, *6*, 6803.
- (37) Li, Y. L.; Wang, J. J.; Li, X. F.; Geng, D. S.; Li, R. Y.; Sun, X. L. *Chem. Comm.* **2011**, *47*, 9438.
- (38) Yan, J.; Wei, T.; Shao, B.; Ma, F. Q.; Fan, Z. J.; Zhang, M. L.; Zheng, C.; Shang, Y. C.; Qian, W. Z.; Wei, F. *Carbon* **2010**, *48*, 1731.
- (39) Park, S. H.; Kim, H. K.; Ahn, D. J.; Lee, S. I.; Roh, K. C.; Kim, K. B. *Electrochim. Commun.* **2013**, *34*, 117.
- (40) Park, S. H.; Bak, S. M.; Kim, K. H.; Jegal, J. P.; Lee, S. I.; Lee, J.; Kim, K. B. *J. Mater. Chem.* **2011**, *21*, 680.